

# Mirror-symmetry protected topological phase in a zigzag ladder with staggered potential

Devendra Singh Bhakuni,<sup>1</sup> Amrita Ghosh,<sup>1,2</sup> and Eytan Grosfeld<sup>1</sup>

<sup>1</sup>*Department of Physics, Ben-Gurion University of the Negev, Beer-Sheva 8410501, Israel*

<sup>2</sup>*Physics Division, National Center for Theoretical Sciences, Taipei 10617, Taiwan*

We study spinless fermions on a zigzag ladder subjected to staggered on-site potential along both of its legs. Three insulating phases, including a charge-density-wave at half-filling, and two dimer insulators at quarter and three-quarter fillings, are identified. The two dimer insulators admit topological phases at opposite signs of the on-site potential, protected by the underlying mirror-symmetry. The phases are characterized by a quantized value of the Zak phase as well as of the entanglement entropy. By performing a projection to the lower and upper two bands separately we show that the system reveals an emergent chiral symmetry. Using density-matrix renormalization group simulations, the topological phases are shown to be remarkably robust against any amount of nearest-neighbor inter-leg as well as intra-leg interactions. Our results are supported by quantum Monte-Carlo simulations in applicable limits of the ladder.

## I. INTRODUCTION

Topological phases of matter have gained enormous interest in condensed matter since their discovery [1, 2]. In particular, topological insulators (TIs) of non-interacting fermions are bulk insulators that, in contrast to their conventional counterparts, admit protected gapless surface states. These surface states are protected by the underlying symmetry of the system, and are robust against any perturbations as long as the symmetries are respected.

Symmetry-protected topological states are mainly categorized into two groups based on the symmetry type: non-spatial symmetries and spatial symmetries. Depending on the non-spatial internal symmetries of the system, such as time-reversal, particle-hole and chiral symmetry, topological phases of non-interacting fermions are classified in a 10-fold symmetry class [3–6]. Apart from this conventional classification, recent studies have shown that lattice symmetries also play a crucial role and can be solely responsible for the protection of certain topological phases. These topological phases, arising from spatial symmetries of the system, are called topological crystalline phases [7–11]. One important member of this spatial symmetry group is mirror-symmetry, which has been demonstrated to give rise to various novel phases [12–22].

While the search for new topological phases is at the forefront of condensed matter research, the investigation of topological crystalline phases and their robustness against various perturbations and many-body interactions is in a nascent stage. Artificially engineered systems, such as cold atoms in optical lattices, provide precise control over the tunable parameters of the system and have become a prolific venue for realizing various phases of non-interacting as well as interacting fermions and bosons [23–33]. Such systems could therefore provide a bridge connecting theoretical proposals and experimental realizations of topological phases.

In this work, we propose and study the properties of a one-dimensional (1D) model of spinless fermions on a zigzag ladder exhibiting topological phases protected by mirror-symmetry. The ladder is subjected to a staggered

on-site potential along both of its legs, and both nearest-neighbor (NN) and next-nearest-neighbor (NNN) hoppings (see Fig. 1). Despite its apparent simplicity, the model gives rise to a rich phase diagram consisting of three insulating phases: a charge-density-wave (CDW) at half-filling and two dimer insulators (DIs) at quarter and three-quarter fillings. The Berry-phase topological invariant as well as the bipartite entanglement entropy identify one of the two DIs as a TI, depending on the sign of the on-site potential. Furthermore, we obtain the projected Hamiltonian in the lower and upper two bands separately which demonstrates an emergent chiral symmetry that pins the edge states in the middle of the respective bands. Using density-matrix renormalization group (DMRG), we find that the topological phases are remarkably robust against any amount of NN as well as NNN interactions. The results are supported by quantum Monte-Carlo (QMC) simulations in the limit of zero NNN hopping, where spinless fermions can be mapped into hard-core bosons.

The paper is organized as follows. In Sec. II we describe the model and introduce the various tools we em-

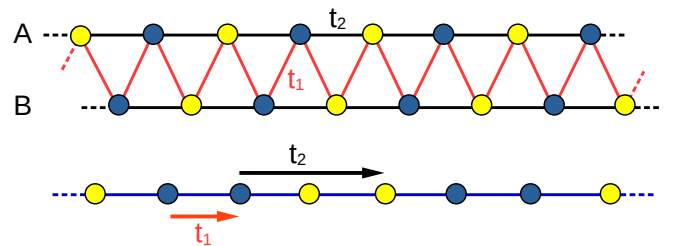


Figure 1. Top: Pictorial description of the zigzag ladder considered in the main text. The indices A and B stand for the two legs of the ladder. The red and black lines represent the NN (inter-leg) and NNN (intra-leg) bonds with hopping strength  $t_1$  and  $t_2$ , respectively. The dashed lines indicate the bonds which connect the ladder across the boundary. Lattice sites denoted by yellow (blue) circles admit on-site potential  $-W$  ( $W$ ). Bottom: Mapping of the zigzag ladder to a 1D chain.

ploy to characterize its topological phases. In Sec. III we detail our characterization considering various settings with zero and non-zero NNN hopping and in the presence of NN and NNN interactions. In Sec. IV we conclude. In App. A we report QMC simulations.

## II. MODEL HAMILTONIAN AND TOPOLOGICAL CHARACTERIZATION

We consider spinless fermions hopping in a zigzag ladder with staggered on-site potential  $W$  applied along its legs  $A$  and  $B$  as depicted in Fig. 1. Each leg of the ladder consists of  $N$  sites. The Hamiltonian of the system can be written as,

$$\begin{aligned} H = & -t_1 \sum_i \left( a_i^\dagger b_i + a_i^\dagger b_{i+1} + \text{H.c.} \right) \\ & - t_2 \sum_i \left( a_i^\dagger a_{i+1} + b_i^\dagger b_{i+1} + \text{H.c.} \right) \\ & - W \sum_i (-1)^i n_i^A + W \sum_i (-1)^i n_i^B. \end{aligned} \quad (1)$$

Here  $a_i^\dagger$  ( $a_i$ ) is the creation (annihilation) operator of a fermion at site  $i$  in leg A and  $b_i^\dagger$  ( $b_i$ ) represents the same in leg B. The operator  $n_i^A = a_i^\dagger a_i$  ( $n_i^B = b_i^\dagger b_i$ ) denotes the number operator at site  $i$  in leg A (B), and  $W$  represents the strength of the on-site potential. The NN (inter-leg) hopping is given by  $t_1$ , while  $t_2$  denotes the NNN (intra-leg) hopping. Under periodic boundary condition (PBC), the Hamiltonian can be written in momentum space as

$$\mathcal{H}(k) = \begin{bmatrix} -W & -t_1 & -t_2\alpha^*(k) & -t_1\beta^*(k) \\ -t_1 & W & -t_1 & -t_2\alpha^*(k) \\ -t_2\alpha(k) & -t_1 & W & -t_1 \\ -t_1\beta(k) & -t_2\alpha(k) & -t_1 & -W \end{bmatrix}, \quad (2)$$

where  $\alpha(k) = 1 + e^{ik}$  and  $\beta(k) = e^{ik}$ . The Hamiltonian  $\mathcal{H}(k)$  is symmetric under the time-reversal operation and also possesses mirror symmetry. Under the time-reversal operation, with  $T$  being the anti-unitary time-reversal operator, the Hamiltonian in Eq. 2 behaves as  $T\mathcal{H}(k)T^{-1} = \mathcal{H}(-k)$ . In this case, the time-reversal operator is simply the complex conjugation operator  $\mathcal{K}$ , i.e.,  $T = \mathcal{K}$ , which satisfies  $T^2 = 1$ . On the other hand, under the mirror symmetry, the Hamiltonian obeys:  $M\mathcal{H}(k)M^{-1} = \mathcal{H}(-k)$  where  $M = \sigma_x \otimes \sigma_x$  is the mirror symmetry operator. Since the two symmetry operators  $T$  and  $M$  commute with each other:  $[T, M] = 0$ , the model is a member of the mirror symmetry class AI [7], which admits a  $\mathbb{Z}$  topological number in 1D.

The topological phase can be characterized by the topological invariant Berry phase, which can be calculated using the Fukui-Hatsugai-Suzuki algorithm [34],

$$\mathbb{Z} = \frac{1}{\pi} \text{Im} \left[ \log \left( \prod_{i=1}^{N_c} \frac{|U^{(i)}|}{\sqrt{|U^{(i)}||U^{(i)*}|}} \right) \right], \quad (3)$$

where the Brillouin zone is discretized in  $N_c = N/2$  unit cells with lattice points  $k_i = -\pi + 2\pi i/N_c$  with  $i = 1, 2, \dots, N_c$  and we have  $k_{N_c+1} \equiv k_1$ . The elements of  $U^{(i)}$  are calculated as  $U_{mn}^{(i)} \equiv \langle \psi_m(k_{i+1}) | \psi_n(k_i) \rangle$ , with  $|\psi_m(k)\rangle$  being the single-particle eigenvectors of  $\mathcal{H}(k)$  participating in the relevant filling, and  $|U^{(i)}|$  denotes the determinant of  $U^{(i)}$ .

In addition to the Berry phase, we characterize the phases using the bipartite entanglement entropy. The entanglement entropy quantifies certain correlation between two subsystems of a composite system  $A \cup B$ . It is defined as  $S_A = -\text{Tr}_B(\rho \log \rho)$ , where  $\rho$  denotes the density matrix of  $A \cup B$  and  $\text{Tr}_B$  represents the partial trace over the subsystem B. The entanglement entropy has been extensively used to characterize various underlying features of both interacting and non-interacting systems including the characterization of quantum phase transitions, topological phase transitions, localization-to-delocalization transitions, and many more [35–42].

For non-interacting particles, a computationally efficient method to calculate the entanglement entropy was demonstrated in Ref. [43]. The method reduces the complexity of the problem by bringing down an exponential dependence on the system size to a polynomial dependence. The procedure constitutes of diagonalization of a two-point correlation matrix,  $C_{mn} \equiv \langle c_m^\dagger c_n \rangle$ , which inherently takes care of the filling factor. Here,  $c_m^\dagger$  ( $c_m$ ) creates (annihilates) a fermion at site  $m$  in the system. The entanglement entropy is then calculated from the eigenvalues of the correlation matrix  $n_i$  as

$$S = - \sum_i [n_i \log n_i + (1 - n_i) \log(1 - n_i)]. \quad (4)$$

While this formulation is limited to the non-interacting case, we use DMRG to study the topological properties in the presence of many-body interactions. The numerical simulations for the interacting case are performed using

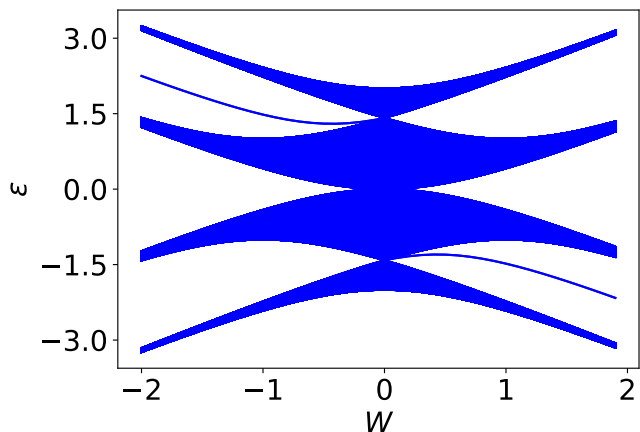


Figure 2. Energy spectrum with OBC with varying values of  $W$ . The calculations are performed on a ladder with  $N = 2000$  sites in each leg, with  $t_1 = 1.0$  and  $t_2 = 0.0$ .

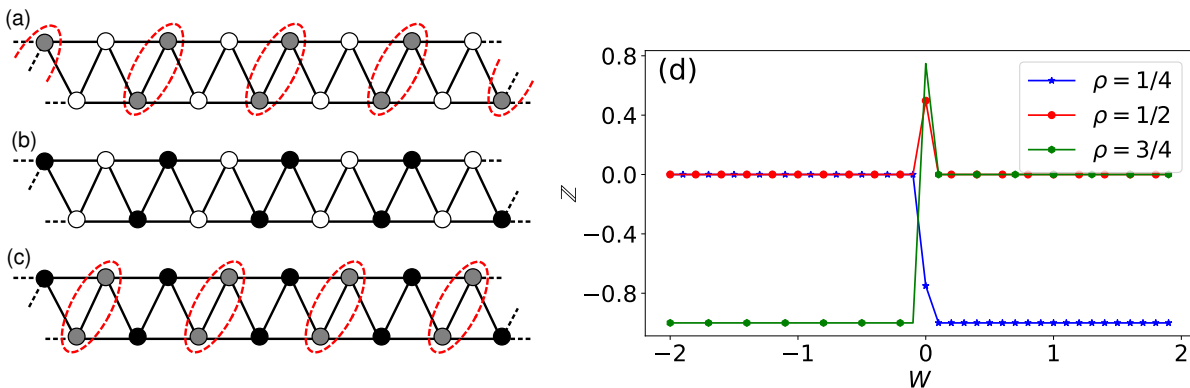


Figure 3. Structures of the three insulating phases of Fig. 2: (a) the dimer insulator at  $\rho = 1/4$ ; (b) the CDW at half-filling; and, (c) the dimer insulator at density  $3/4$ . The white (black) circles denote empty (filled) sites with density  $0.0(1.0)$ , whereas the grey circles signify half-filled sites with density  $0.5$ . The red dashed curves represent the formation of dimers. (d) The corresponding Berry phase as a function of  $W$  for filling fractions  $1/4$ ,  $1/2$  and  $3/4$  with  $t_1 = 1.0$  and  $t_2 = 0.0$ .

the TeNPy Library [44].

### III. RESULTS AND DISCUSSION

#### A. Zero NNN hopping

We first consider the Hamiltonian in Eq. 1 without the NNN coupling by setting  $t_2 = 0$ . The energy spectrum as a function of  $W$  under the open boundary condition (OBC) is shown in Fig. 2. The spectrum mainly consists of three gapped phases, corresponding to densities  $1/4$ ,  $1/2$ , and  $3/4$ . Interestingly, as the sign of  $W$  is changed from negative to positive, an edge state appears in the middle of the energy-gap at density  $\rho = 1/4$  indicating a trivial-to-topological phase transition at  $W = 0$ . This scenario is reversed for the insulator at density  $3/4$ , where a topological to trivial phase transition occurs on changing the sign of the potential strength  $W$ . However, the insulator at half-filling remains trivial throughout.

In the absence of NNN hopping, the system of spinless fermions can be mapped onto a system of hard-core bosons (HCBs). In order to characterize the three above-mentioned insulating phases and investigate their underlying structures, we employ Stochastic Series Expansion (SSE) QMC [45, 46] on the HCB system and study the following order parameters as defined in App. A: the average HCB density  $\rho$ ; the structure factor  $S(Q)$ ; and, the dimer structure factor  $S_D(Q)$ . The results obtained from QMC calculations, as detailed in App. A, disclose Fig. 3(a),(b) and (c) as the underlying structure of the three insulating phases and the origin of these structures can be understood in the following manner.

In the presence of a staggered potential, half of the lattice sites in the system (depicted by yellow circles in Fig. 1) have lower on-site potential ( $-W$ ) compared to the other half. Therefore, upto half-filling the particles prefer to occupy the lower-potential sites. At  $1/4$ -filling, it is energetically favorable for the system to form dimers occupying the two sites in each red dashed curve in Fig.

3(a), so that the particle can further lower the energy of the system by hopping back and forth between these two sites. For a finite system, this leads to two edge states at  $\rho = 1/4$ .

For the case of half-filling, all sites with on-site potential  $-W$  are completely filled, resulting in a charged-density wave (CDW) structure as shown in Fig. 3(b). Finally, at  $3/4$ -filling the sites with lower on-site potential are completely filled and the rest are half-filled. Now the particles at these half-filled sites hop back and forth between the two NN sites inside each red curve and form dimers as depicted in Fig. 3(c). It is important to note that there is a major difference between the structures of the two DIs. In case of the dimer insulator at  $1/4$ -filling there exists a dimer which involves two edge sites under OBC. Consequently, for  $W > 0$  this dimer insulator displays the existence of edge states as depicted in Fig. 2. However, for the case of  $\rho = 3/4$ , the dimers are entirely formed in the bulk and the edge state does not appear when OBCs are applied. We should note that when the sign of the on-site potential is reversed, the appearance of edge states is also changed. In this situation, the dimer insulator at  $\rho = 1/4$  contains bulk dimers only, whereas the insulator at  $3/4$ -filling shows edge states.

The topological invariants corresponding to densities  $1/4$ ,  $1/2$  and  $3/4$ , are shown in Fig. 3(d) as a function of  $W$ . One can see that for the insulator at  $\rho = 1/4$ , the Berry phase is quantized at  $-1$  for positive values of  $W$ , whereas for negative values of  $W$ , it remains zero. The situation is reversed for the insulator at density  $3/4$ . In this case, the Berry phase remains zero for all positive values of  $W$  and quantized at  $-1$  for negative  $W$  values. Thus we can identify the DIs at  $\rho = 1/4$  and  $\rho = 3/4$  as TIs for  $W > 0$  and  $W < 0$ , respectively. On the other hand, for the insulator at  $\rho = 1/2$ , the Berry phase remains zero throughout for all values of  $W$ , which makes it topologically trivial.

The presence of these distinct phases and the edge states can also be characterized by studying the bipartite entanglement entropy of the ground state. We consider

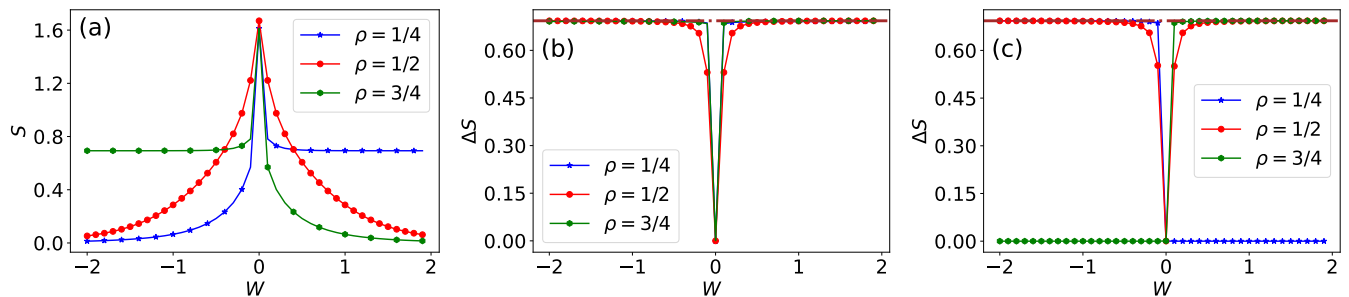


Figure 4. (a) Entanglement entropy as a function of  $W$  for filling fractions 1/4, 1/2 and 3/4 with OBC. (b,c)  $\Delta S$  as a function of  $W$  for PBC and OBC respectively. The other parameters are:  $N = 2000$ ,  $t_1 = 1.0$ , and  $t_2 = 0.0$ .

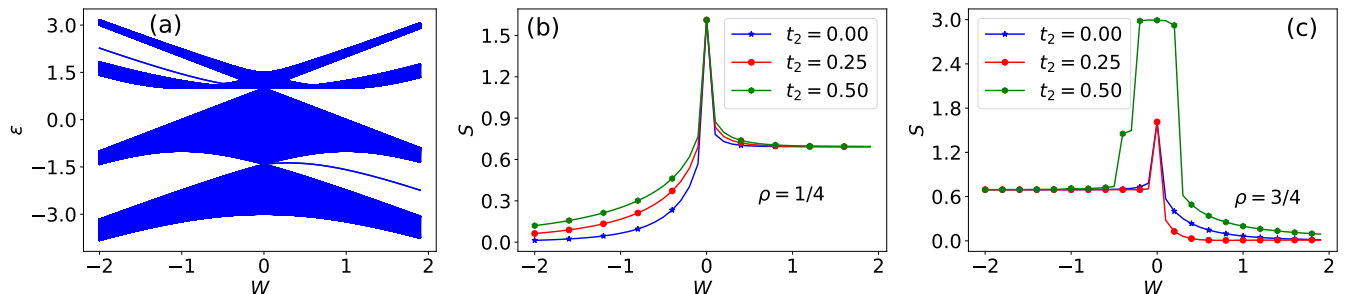


Figure 5. (a) Energy spectrum as a function of  $W$  for a non-zero NNN hopping  $t_2 = 0.5$ . (b,c) Entanglement entropy as a function of  $W$  for different values of NNN hopping  $t_2$  with PBC: (b) for  $\rho = 1/2$ ; (c) for  $\rho = 3/4$ . Here  $N = 2000$  and  $t_1 = 1.0$ .

the left and right parts of the ladder, constituting an equal number of sites, as two sub-systems. The entanglement entropy for different filling factors with OBC is plotted in Fig.4(a). For  $\rho = 1/4$ , the entanglement entropy increases with increasing  $W$  indicating a signature of quantum phase transition at  $W = 0$ , after which it saturates to  $\ln 2$  in the topological phase. A reverse trend can be seen for  $\rho = 3/4$  where the topological phase exists for  $W < 0$ . On the other hand, for  $\rho = 1/2$ , we see a symmetric pattern. To observe the signature of edge state, we calculate the change in the entanglement entropy when an additional particle is either added or removed. We define the quantity  $\Delta S_\rho^{(\pm 1)}$  as [42]

$$\Delta S_\rho^{(\pm 1)} = S_\rho^{(\pm 1)} - S_\rho, \quad (5)$$

where  $S_\rho$  is the entanglement entropy at filling factor  $\rho$  and  $S_\rho^{(\pm 1)}$  is the same but with a single particle either added or removed. For our calculation, the difference  $\Delta S \equiv \Delta S_\rho^{(-1)}$  is calculated by considering the entanglement entropy at  $\rho = 1/4$ ,  $1/2$ , and  $3/4$ , and then removing a single particle from these filling factors. The behavior of  $\Delta S$  as function of  $W$  is plotted in Fig. 4(b,c). While under PBC (Fig. 4(b)) the behavior remains the same for all the filling factors, the case of OBC (Fig. 4(c)) shows similar behavior as that of the Berry phase (Fig. 3(d)). Specifically, for  $\rho = 1/4$ , we see a transition from  $\Delta S = \ln 2$  at  $W < 0$  to  $\Delta S = 0$  at  $W > 0$ ; and, for  $\rho = 3/4$ , the trend reverses and a transition from  $\Delta S = 0$  to  $\Delta S = \ln 2$  is observed. These

transitions are taken to signify the presence of edge states for these filling factors. In contrast, for  $\rho = 1/2$ , the behavior of  $\Delta S$  is similar for OBC and PBC, suggesting a trivial phase at this filling factor.

## B. Non-zero NNN hopping

We now consider the case of non-zero NNN hopping. The energy spectrum for  $t_1 = 1.0$  with  $t_2 = 0.5$  as a function of  $W$  is plotted in Fig. 5(a). It can be seen that while the edge state for the filling  $\rho = 1/4$  remains almost unchanged in the presence of a non-zero  $t_2$ , a gapless phase appears at 3/4-filling for small values of  $W$ . The same observation can also be seen from the entanglement entropy plotted in Fig. 5(b,c) for different values of  $t_2$ . For the case of  $\rho = 1/4$ , we see that the behavior of the entanglement entropy is qualitatively similar for different values of  $t_2$  (Fig. 5(b)) which suggests that the topological phase in this filling remains unaffected by  $t_2$ . For  $\rho = 3/4$ , the quantization of the entanglement entropy and appearance the topological phase shifts to larger values of  $|W|$  with increasing  $t_2$  (Fig. 5(c)). The topological phase, however, remains stable for large enough value of the staggered potential  $W$ . The robustness of these topological phases at  $\rho = 1/4$  and  $\rho = 3/4$  can be explained by the presence of an emergent symmetry.

While the Hamiltonian in Eq. (1) admits a mirror symmetry which protects the topological phases, there is no

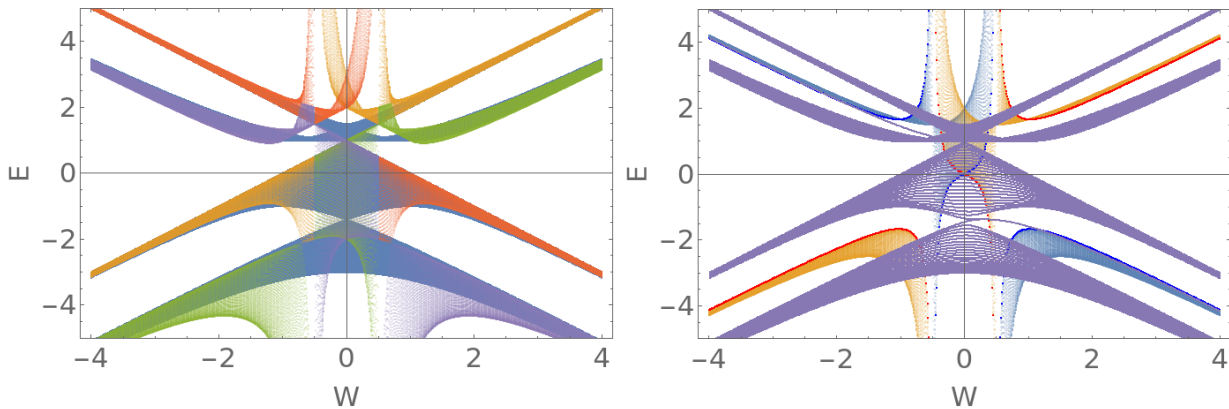


Figure 6. Comparison between the exact spectrum and the spectrum obtained from the projected Hamiltonian. Left panel: the exact spectrum for PBC (blue) and for the lower and upper projected two bands (red, orange, green, purple) as function of  $W$ . Right panel: the spectrum for OBC (purple) and the dispersing centers  $\varepsilon_0(k)$  (blue) and  $\varepsilon'_0(k)$  (orange) with  $k = \pi$  highlighted (bright blue and red respectively). Here  $t_1 = 1.0$ ,  $t_2 = 0.5$ , and  $N = 50$ .

chiral symmetry in the system. However one can show that there is indeed an emergent chiral symmetry, for the lower and upper bands separately, which pins the edge states to the center of the respective bands. By a projection to the lower two bands of the system for  $W > 0$  (or the upper ones for  $W < 0$ ), we can write an effective Hamiltonian

$$\hat{H}_{\text{proj}} = \varepsilon_0(k)\tau_0 + \varepsilon_x(k)\tau_x + \varepsilon_y(k)\tau_y, \quad (6)$$

with

$$\varepsilon_0(k) = -W - \frac{2t_1^2W + 2t_2(t_1^2 + 2t_2W)(1 + \cos k)}{4W^2 - t_1^2}, \quad (7)$$

$$\varepsilon_x(k) = -t_1 \left[ \cos k + \frac{t_1^2 + 2t_2 \cos k (t_2(1 + \cos k) + 2W)}{4W^2 - t_1^2} \right], \quad (8)$$

$$\varepsilon_y(k) = -t_1 \left[ \sin k + \frac{2t_2 \sin k (t_2(1 + \cos k) + 2W)}{4W^2 - t_1^2} \right]. \quad (9)$$

In Eq. (6)  $\tau_0$  is the  $2 \times 2$  identity matrix and  $\tau_i$  ( $i = x, y, z$ ) is the  $i$ 'th Pauli matrix. The resulting bands are plotted in Fig. 6 (left panel, purple and red), matching quite well with the exact spectrum for larger values of  $|W|$ . The projected Hamiltonian of the lower two bands reveals a partial chiral symmetry  $\tau_z$  manifesting a particle-hole symmetry with respect to  $\varepsilon_0(k)$ . Moreover, it has a topological number for both positive and negative larger values of  $W$ . Consequently, it admits an edge state which gets pinned at the middle of the band gap at  $1/4$ -filling for positive  $W$  and at  $3/4$  filling for negative  $W$ . While the center of the band is dispersing with energy  $\varepsilon_0(k)$ , the edge state gets locked to  $k = \pi$  as demonstrated in Fig. 6, right panel.

Performing a similar projection to the upper two bands for  $W > 0$  (or the lower ones for  $W < 0$ ), we get the

projected Hamiltonian

$$\hat{H}'_{\text{proj}} = \varepsilon'_0(k)\tau_0 + \varepsilon'_x(k)\tau_x + \varepsilon'_y(k)\tau_y, \quad (10)$$

where the expressions of  $\varepsilon'_0(k)$ ,  $\varepsilon'_x(k)$  and  $\varepsilon'_y(k)$  in this case reduce to,

$$\varepsilon'_0(k) = W + \frac{(2t_1^2W + 2t_2(2t_2W - t_1^2)(1 + \cos k))}{4W^2 - t_1^2}, \quad (11)$$

$$\varepsilon'_x(k) = -t_1 \left[ 1 + \frac{(t_1^2 \cos k + 2t_2(t_2 - 2W)(1 + \cos k))}{4W^2 - t_1^2} \right], \quad (12)$$

$$\varepsilon'_y(k) = -t_1 \frac{(t_1^2 - 4t_2W) \sin k}{4W^2 - t_1^2}. \quad (13)$$

The resulting bands are plotted in Fig. 6 (left panel, green and orange). Therefore the projected Hamiltonian for the upper two bands also admits a chiral symmetry  $\tau_z$  manifesting a particle-hole symmetry with respect to  $\varepsilon'_0(k)$ . In contrast to the previous case, this Hamiltonian has no topological number in its regions of validity.

### C. Effect of interactions

We now study the stability of the TIs in the presence of many-body interactions. To demonstrate the effect of interactions we choose the TI at density  $1/4$ ; however, we have confirmed that the TI at  $\rho = 3/4$  behaves exactly the same way. We consider a NN repulsion between the fermions by adding the following term to the Hamiltonian in Eq. (1),

$$H_1 = V_1 \sum_i (n_i^A n_i^B + n_i^A n_{i+1}^B). \quad (14)$$

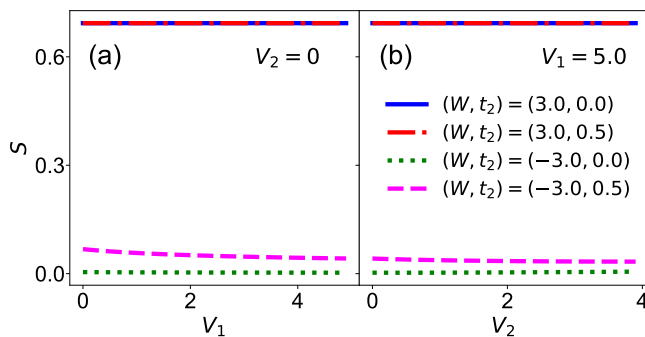


Figure 7. Entanglement entropy  $S$  as a function of : (a) NN repulsion  $V_1$  with  $V_2 = 0$ ; and, (b) NNN repulsion  $V_2$  with  $V_1 = 5.0$ , both measured under OBC. The measurements are performed for four different sets of  $(W, t_2)$  values detailed in the legend with  $N = 400$ .

Fig. 7(a) shows the variation of the entanglement entropy  $S$  as we tune the NN repulsion strength  $V_1$ . We consider various different sets of  $(W, t_2)$  values. As mentioned previously, for  $V_1 = 0$ , the insulator at  $\rho = 1/4$  is topological (non-topological) in nature for  $W > 0$  ( $W < 0$ ), for both zero and nonzero values of  $t_2$ . We see that in the presence of NN repulsion, the topological nature of the insulator at  $\rho = 1/4$  remains unaltered as  $S$  remains quantized at  $\ln 2$  for all values of  $V_1$  (Fig. 7(a)). In contrast, for  $W < 0$ , the topologically trivial insulator remains the same as a function of increasing  $V_1$  with a vanishingly small value of the entanglement entropy. In fact, one can argue that the topological nature of the insulator at  $\rho = 1/4$  will be protected against any amount of NN repulsion. Since the dimers in the  $\rho = 1/4$  dimer insulator are formed at every fourth NN bond, the particles forming two neighboring dimers do not feel any repulsion among them. As a result, the NN repulsion does not interrupt the hopping process necessary to form dimers. Thus, the topological nature of the dimer insulator remains intact and unaffected in the presence of any amount of NN repulsion.

We next consider the effect of NNN repulsion by adding another term in the Hamiltonian, given by,

$$H_2 = V_2 \sum_i (n_i^A n_{i+1}^A + n_i^B n_{i+1}^B). \quad (15)$$

In Fig. 7(b) we show the variation of the entanglement

entropy  $S$  as a function of the NNN repulsion strength  $V_2$  for a fixed value of NN repulsion,  $V_1 = 5$ . We see that the effect of NNN repulsion on the dimer insulator is similar to the effect of NN repulsion. Since the entanglement entropy remains quantized at  $\ln 2$  with varying  $V_2$ , the topological nature of the insulator is robust against the NNN repulsion. As the dimers are formed on every fourth NN bond, the fermions on two neighboring dimers are shielded from the NNN repulsion. Therefore, similarly to the case of NN repulsion, the TI is robust against any amount of NNN repulsion as well.

#### IV. CONCLUSION

To conclude, we have considered spinless fermions, with NN as well as NNN hopping, on a zigzag ladder subjected to staggered on-site potential along its two legs. The system reveals the existence of three gapped phases at  $1/4$ ,  $1/2$  and  $3/4$  filling-fractions. The insulator at  $1/2$ -filling turns out to be a CDW in nature, whereas the other two gapped phases are characterized as DIs. One of these two DIs emerges as a TI, depending on the sign of the on-site potential  $W$ . We have characterized the topological nature of these insulators using the Berry phase as well as entanglement entropy. The topological phase is protected by mirror-symmetry which places the system in the AI mirror-symmetry class. Additionally, performing a projection to the lower and upper two bands separately, we have shown that the system admits an emergent chiral symmetry which pins the edge states of the TIs to the middle of the corresponding energy bands. Interestingly, the TIs observed in our system are robust against any amount of NN as well as NNN repulsion. Since the dimers formed in the system are well-separated from each other, the topological phases become stable even with longer-range interactions.

#### ACKNOWLEDGEMENT

This research was funded by the Israel Innovation Authority under the Kamin program as part of the QuantERA project InterPol, and by the Israel Science Foundation under grant 1626/16. DSB and AG thank the Kreitman School of Advanced Graduate Studies for support. AG would also like to thank Ministry of Science and Technology, National Center for Theoretical Sciences of Taiwan for support towards the end of this project.

[1] M. Z. Hasan and C. L. Kane, Colloquium: Topological insulators, *Reviews of Modern Physics* **82**, 3045 (2010).  
 [2] X.-L. Qi and S.-C. Zhang, Topological insulators and superconductors, *Rev. Mod. Phys.* **83**, 1057 (2011).  
 [3] A. Altland and M. R. Zirnbauer, Nonstandard symmetry classes in mesoscopic normal-superconducting hybrid structures, *Phys. Rev. B* **55**, 1142 (1997).

[4] A. P. Schnyder, S. Ryu, A. Furusaki, and A. W. W. Ludwig, Classification of topological insulators and superconductors in three spatial dimensions, *Phys. Rev. B* **78**, 195125 (2008).  
 [5] A. P. Schnyder, S. Ryu, and A. W. W. Ludwig, Lattice model of a three-dimensional topological singlet superconductor with time-reversal symmetry, *Phys. Rev. Lett.* **102**, 196804 (2009).

- [6] C.-K. Chiu, J. C. Y. Teo, A. P. Schnyder, and S. Ryu, Classification of topological quantum matter with symmetries, *Reviews of Modern Physics* **88**, 035005 (2016).
- [7] C.-K. Chiu, H. Yao, and S. Ryu, Classification of topological insulators and superconductors in the presence of reflection symmetry, *Phys. Rev. B* **88**, 075142 (2013).
- [8] Y. Ando and L. Fu, Topological crystalline insulators and topological superconductors: From concepts to materials, *Annual Review of Condensed Matter Physics* **6**, 361 (2015).
- [9] D. V. Else and R. Thorngren, Crystalline topological phases as defect networks, *Phys. Rev. B* **99**, 115116 (2019).
- [10] L. Fu, Topological Crystalline Insulators, *Phys. Rev. Lett.* **106**, 106802 (2011).
- [11] K. Shiozaki and M. Sato, Topology of crystalline insulators and superconductors, *Phys. Rev. B* **90**, 165114 (2014).
- [12] J. C. Y. Teo, L. Fu, and C. L. Kane, Surface states and topological invariants in three-dimensional topological insulators: Application to  $\text{Bi}_{1-x}\text{Sb}_x$ , *Phys. Rev. B* **78**, 045426 (2008).
- [13] T. H. Hsieh, H. Lin, J. Liu, W. Duan, A. Bansil, and L. Fu, Topological crystalline insulators in the snite material class, *Nature Communications* **3**, 982 (2012).
- [14] S.-Y. Xu, C. Liu, N. Alidoust, M. Neupane, D. Qian, I. Belopolski, J. D. Denlinger, Y. J. Wang, H. Lin, L. A. Wray, G. Landolt, B. Slomski, J. H. Dil, A. Marcinkova, E. Morosan, Q. Gibson, R. Sankar, F. C. Chou, R. J. Cava, A. Bansil, and M. Z. Hasan, Observation of a topological crystalline insulator phase and topological phase transition in  $\text{Pb}_{1-x}\text{Sn}_x\text{Te}$ , *Nature Communications* **3**, 1192 (2012).
- [15] Y. Tanaka, Z. Ren, T. Sato, K. Nakayama, S. Souma, T. Takahashi, K. Segawa, and Y. Ando, Experimental realization of a topological crystalline insulator in  $\text{SnTe}$ , *Nature Physics* **8**, 800 (2012).
- [16] P. Dziawa, B. J. Kowalski, K. Dybko, R. Buczko, A. Szczerbakow, M. Szot, E. Łusakowska, T. Balasubramanian, B. M. Wojek, M. H. Berntsen, O. Tjernberg, and T. Story, Topological crystalline insulator states in  $\text{Pb}_{1-x}\text{Sn}_x\text{Se}$ , *Nature Materials* **11**, 1023 (2012).
- [17] F. Zhang, C. L. Kane, and E. J. Mele, Topological mirror superconductivity, *Phys. Rev. Lett.* **111**, 056403 (2013).
- [18] Y. Ueno, A. Yamakage, Y. Tanaka, and M. Sato, Symmetry-protected majorana fermions in topological crystalline superconductors: Theory and application to  $\text{Sr}_2\text{RuO}_4$ , *Phys. Rev. Lett.* **111**, 087002 (2013).
- [19] T. Morimoto and A. Furusaki, Topological classification with additional symmetries from clifford algebras, *Phys. Rev. B* **88**, 125129 (2013).
- [20] K. Shiozaki and M. Sato, Topology of crystalline insulators and superconductors, *Phys. Rev. B* **90**, 165114 (2014).
- [21] R. Okugawa and T. Yokoyama, Generic phase diagram for weyl superconductivity in mirror-symmetric superconductors, *Phys. Rev. B* **97**, 060504 (2018).
- [22] A. Ghosh and E. Grosfeld, Weak topological insulating phases of hard-core-bosons on the honeycomb lattice, *SciPost Phys.* **10**, 59 (2021).
- [23] N. Goldman, J. C. Budich, and P. Zoller, Topological quantum matter with ultracold gases in optical lattices, *Nature Phys* **12**, 639 (2016).
- [24] M. Aidelsburger, M. Lohse, C. Schweizer, M. Atala, J. Barreiro, S. Nascimbène, N. Cooper, I. Bloch, and N. Goldman, Measuring the Chern number of Hofstadter bands with ultracold bosonic atoms, *Nature Phys* **11**, 162 (2015).
- [25] I. Bloch, J. Dalibard, and S. Nascimbène, Quantum simulations with ultracold quantum gases, *Nature Phys* **8**, 267 (2012).
- [26] N. Cooper, J. Dalibard, and I. Spielman, Topological bands for ultracold atoms, *Rev. Mod. Phys.* **91**, 015005 (2019).
- [27] M. Aidelsburger, M. Atala, M. Lohse, J. T. Barreiro, B. Paredes, and I. Bloch, Realization of the Hofstadter Hamiltonian with Ultracold Atoms in Optical Lattices, *Phys. Rev. Lett.* **111**, 185301 (2013).
- [28] H. Miyake, G. A. Siviloglou, C. J. Kennedy, W. C. Burton, and W. Ketterle, Realizing the Harper Hamiltonian with Laser-Assisted Tunneling in Optical Lattices, *Phys. Rev. Lett.* **111**, 185302 (2013).
- [29] M. E. Tai, A. Lukin, M. Rispoli, R. Schittko, T. Menke, Dan Borgnia, P. M. Preiss, F. Grusdt, A. M. Kaufman, and M. Greiner, Microscopy of the interacting Harper–Hofstadter model in the two-body limit, *Nature* **546**, 519 (2017).
- [30] G. Jotzu, M. Messer, R. Desbuquois, M. Lebrat, T. Uehlinger, D. Greif, and T. Esslinger, Experimental realization of the topological Haldane model with ultracold fermions, *Nature* **515**, 237 (2014).
- [31] N. Fläschner, B. S. Rem, M. Tarnowski, D. Vogel, D.-S. Lühmann, K. Sengstock, and C. Weitenberg, Experimental reconstruction of the berry curvature in a floquet bloch band, *Science* **352**, 1091 (2016).
- [32] B. K. Stuhl, H.-I. Lu, L. M. Ayccock, D. Genkina, and I. B. Spielman, Visualizing edge states with an atomic bose gas in the quantum hall regime, *Science* **349**, 1514 (2015).
- [33] M. Mancini, G. Pagano, G. Cappellini, L. Livi, M. Rider, J. Catani, C. Sias, P. Zoller, M. Inguscio, M. Dalmonte, and L. Fallani, Observation of chiral edge states with neutral fermions in synthetic hall ribbons, *Science* **349**, 1510 (2015).
- [34] T. Fukui, Y. Hatsugai, and H. Suzuki, Chern Numbers in Discretized Brillouin Zone: Efficient Method of Computing (Spin) Hall Conductances, *Journal of the Physical Society of Japan* **74**, 1674 (2005).
- [35] F. Pollmann, A. M. Turner, E. Berg, and M. Oshikawa, Entanglement spectrum of a topological phase in one dimension, *Phys. Rev. B* **81**, 064439 (2010).
- [36] A. M. Turner, F. Pollmann, and E. Berg, Topological phases of one-dimensional fermions: An entanglement point of view, *Phys. Rev. B* **83**, 075102 (2011).
- [37] H. Li and F. D. M. Haldane, Entanglement spectrum as a generalization of entanglement entropy: Identification of topological order in non-abelian fractional quantum hall effect states, *Phys. Rev. Lett.* **101**, 010504 (2008).
- [38] N. Lambert, C. Emary, and T. Brandes, Entanglement and the phase transition in single-mode superradiance, *Phys. Rev. Lett.* **92**, 073602 (2004).
- [39] J. H. Bardarson, F. Pollmann, and J. E. Moore, Unbounded growth of entanglement in models of many-body localization, *Phys. Rev. Lett.* **109**, 017202 (2012).
- [40] J. Sirker, M. Maiti, N. P. Konstantinidis, and N. Sedlmayr, Boundary fidelity and entanglement in the symmetry protected topological phase of the SSH model, *Jour-*

nal of Statistical Mechanics: Theory and Experiment **2014**, P10032 (2014).

- [41] J. Cho and K. W. Kim, Quantum phase transition and entanglement in topological quantum wires, *Scientific Reports* **7**, 2745 (2017).
- [42] R. Nehra, D. S. Bhakuni, S. Gangadharaiyah, and A. Sharma, Many-body entanglement in a topological chiral ladder, *Phys. Rev. B* **98**, 045120 (2018).
- [43] I. Peschel and V. Eisler, Reduced density matrices and entanglement entropy in free lattice models, *Journal of Physics A Mathematical General* **42**, 504003 (2009).
- [44] J. Hauschild and F. Pollmann, Efficient numerical simulations with Tensor Networks: Tensor Network Python (TeNPy), *SciPost Phys. Lect. Notes*, 5 (2018).
- [45] A. W. Sandvik, Finite-size scaling of the ground-state parameters of the two-dimensional Heisenberg model, *Phys. Rev. B* **56**, 11678 (1997).
- [46] A. Sandvik, Lecture notes for course given at the 14th training course in physics of strongly correlated systems, salerno (vietri sul mare), italy (2010).

### Appendix A: QMC calculations

In this section we detail the QMC calculations and results obtained therefrom, for a system of HCBs obeying the Hamiltonian given in Eq. (1), in the absence of NNN hopping. First, we describe the three order parameters used in QMC calculations, namely: the average HCB density  $\rho$ , the structure factor  $S(Q)$ , and the dimer structure factor  $S_D(Q)$ .

The average density of a system containing  $N_s$  sites can be calculated as

$$\rho = \frac{1}{N_s} \sum_i n_i, \quad (\text{A1})$$

where  $n_i$  gives the number of HCBs (either 0 or 1) at site  $i$ .

The structure factor per site can be calculated as,

$$S(Q) = \frac{1}{N_s^2} \sum_{i,j} e^{iQ(r_i - r_j)} \langle n_i n_j \rangle, \quad (\text{A2})$$

where  $\langle \dots \rangle$  represents ensemble average and  $r_i$  denotes the position of site  $i$ . The zigzag ladder can always be represented as a one-dimensional chain by straightening the red bonds (bottom panel of Fig. 1 in the main text). In the above expression for the structure factor we use the position vectors of this transformed 1D chain and its corresponding momentum values as  $Q$ .

Next, the dimer structure factor is defined as

$$S_D(Q) = \frac{1}{N_b^2} \sum_{\alpha,\beta} e^{iQ(R_\alpha - R_\beta)} \langle D_\alpha D_\beta \rangle, \quad (\text{A3})$$

where  $R_\alpha$  denote the midpoints of the NN bonds of the transformed 1D chain and the dimer operator  $D_\alpha = d_{\alpha_L}^\dagger d_{\alpha_R} + d_{\alpha_R}^\dagger d_{\alpha_L}$  is defined on the  $\alpha$ -th NN bond. Here  $\alpha_L$  and  $\alpha_R$  represent the two lattice sites attached to

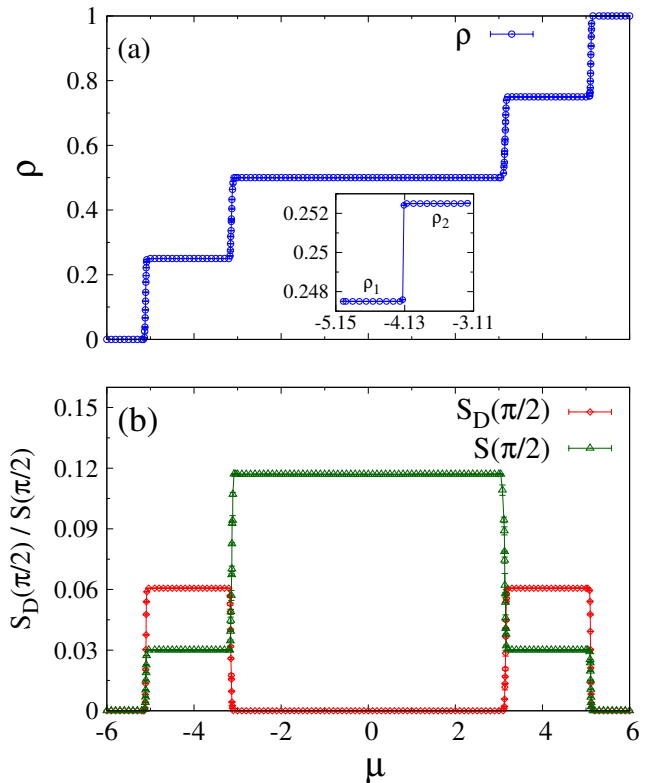


Figure 8. Variations of the order parameters: (a) HCB density  $\rho$  and (b) structure factor  $S(\frac{\pi}{2})$  and dimer structure factor  $S_D(\frac{\pi}{2})$ , as a function of the chemical potential  $\mu$ . Inset of (a): Splitting of  $\rho = 1/4$  plateau under OBC. The measurements are done on a ladder with  $N = 200$ , where  $t_1 = 1.0$ ,  $t_2 = 0.0$  and  $W = 4.0$ .

this bond and  $d_{\alpha_L}^\dagger (d_{\alpha_L})$  and  $d_{\alpha_R}^\dagger (d_{\alpha_R})$  create(annihilate) a HCB at these two sites, respectively. The summation in the above expression runs over the NN bonds in order to detect the formation of dimers along these bonds only.

Fig. 8 displays the variations of the order parameters, namely the HCB density  $\rho$ , structure factor  $S(\pi/2)$  and dimer structure factor  $S_D(\pi/2)$  as a function of the chemical potential  $\mu$  for a fixed value of onsite potential strength  $W = 4$ . Here we have set the NN and NNN hopping to be  $t_1 = 1.0$  and  $t_2 = 0.0$ , respectively. It is clear from Fig. 3(a) that in the absence of NNN hopping, there exists three incompressible insulating phases corresponding to the three plateaus. To characterize the nature of these insulators we have calculated the dimer structure factor  $S_D(Q)$  and structure factor  $S(Q)$  for all values of  $Q$  and identify  $Q = \pi/2$  to be the one at which both of them peak. Fig. 3(b) displays the change in  $S_D(\pi/2)$  and  $S(\pi/2)$  as we tune the chemical potential of the system. The dimer structure factor shows a peak at densities  $1/4$  and  $3/4$  with a value very close to  $0.0625$ , whereas the structure factor attains a value close to  $0.125$  at half-filling. The structures of the three above-mentioned insulating phases are shown in Fig. 1(a),(b) and (c). In terms of the transformed 1D lattice, both of the DIs consist of



dimers at every fourth NN bond. Therefore in Fig. 8 the dimer structure factor peaks at  $Q = \pi/2$  with a value 0.0625. On the other hand for the CDW at half-filling the sites in the red dashed curve corresponding to dimers in Fig. 3 become completely filled, while the rest of the sites are empty. Therefore, for this structure the dimer structure factor vanishes completely and the structure factor attains the maximum value 0.125 at wavevector  $Q = \pi/2$  as depicted in Fig. 8.

In QMC calculations the existence of the edge states is manifested in the following way. For  $W > 0$ , under OBC the variation of the average HCB density  $\rho$  as a function of the chemical potential  $\mu$  remains unchanged except for  $\rho = 1/4$ . For a ladder with  $N = 200$  sites in

each leg, the plateau at 1/4-filling with PBC splits into two plateaus corresponding to densities  $\rho_1 = 0.2475$  and  $\rho_2 = 0.2525$  once we open the boundary of the system (inset of Fig. 8(a)). The values of  $\rho_1$  and  $\rho_2$  depend on the size of the system. For a system with  $2N$  total number of sites, the plateau at density  $\rho$  splits into  $\rho_1 = \rho - 1/(2N)$  and  $\rho_2 = \rho + 1/(2N)$ , such that  $(\rho_2 - \rho_1) \times 2N = 2$  gives the number of edge states in the system. Therefore the splitting of the plateau under OBC proves the existence of the edge states in the system. The lower plateau ( $\rho_1$ ) corresponds to a situation when both of the edge sites are empty, while the upper plateau ( $\rho_2$ ) signifies a situation when both of them are occupied.